Near conductive cooling rates in the upper-plutonic section of crust formed at the East Pacific

Kathrin Faak, Laurence A. Coogan, Sumit Chakraborty

2015

Citation for this paper:

Faak, K., Coogan, L.A. & Chakraborty, S. (2015). Near conductive cooling rates in the upper-plutonic section of crust formed at the East Pacific. *Earth and Planetary Science Letters, 423,* 36-47. https://doi.org/10.1016/j.epsl.2015.04.025

Near conductive cooling rates in the upper-plutonic section of crust formed at the East Pacific Rise

Kathrin Faak[1,2], Laurence A. Coogan[2], Sumit Chakraborty[1]

[1] Institut fuer Geologie, Mineralogie und Geophysik,
Ruhr-Universitaet Bochum, Universitaetsstr. 150, D-44801 Germany

[2] School of Earth & Ocean Science, University of Victoria, PO BOX 1700 STN CSC,
Victoria, BC, V8W 2Y2, Canada

corresponding author: Kathrin Faak
present address: 1
Kathrin.Faak@rub.de
Phone: +49 234 32 23228

Abstract

A new geospeedometer, based on diffusion modeling of Mg in plagioclase, is used to determine cooling rates of the upper section of the lower oceanic crust formed at fast-spreading mid-ocean ridges. The investigated natural sample suites include gabbroic rocks formed at three different locations along the fast-spreading East Pacific Rise. These samples cover a depth interval of 0-840 m below the sheeted dike/gabbro boundary and therefore allow the variation of cooling rate as a function of depth within the upper plutonic sequence to be determined. We demonstrate that the cooling rates we obtained are robust (reproducible and consistent across different vertical sections at fast spreading ridges) and decrease significantly with increasing sample depth (covering almost 4 orders of magnitude, ranging from ~1 °Cy^{-1} for the shallowest samples to 0.0003°Cy^{-1} for the deepest samples). Both the absolute cooling rates, and the rate of decrease of cooling rate with depth, are consistent with conductive thermal models. In contrast, the absolute cooling rates determined from the deeper samples (>300 m below DGB), and the large decrease in cooling rate with depth are inconsistent with thermal models that include substantial cooling by off-axis hydrothermal circulation within the upper plutonic section of the crust.

Keywords: *cooling rate, oceanic crust, mid-ocean ridge, diffusion modeling, Mg-in-plagioclase*

1. Introduction

The observation that only a small (~1 km wide and ~50 m deep) axial magma lens (AML) overlies a zone of low seismic velocities (LVZ), that is interpreted to be a crystal mush zone (e.g. Detrick et al., 1987; Dunn et al., 2000), at fast spreading oceanic ridges has posed a conundrum: how is the large volume of the plutonic section of the oceanic crust generated from such a small magma chamber? Two end-member models – the gabbro-glacier model (Quick and Denlinger, 1993; Henstock et al., 1993; Phipps Morgan and Chen, 1993; Fig. 1a) and the sheeted sill model (Kelemen et al., 1997; Korenaga and Kelemen, 1997; Fig. 1b) – were proposed early on to try to address this problem. Each model has its own set of geochemical (e.g. fractionation trends), structural (e.g. pattern of distribution of fabric) and geophysical (e.g. seismic or thermal) implications.

The thermal structure of mid-ocean ridges has long been known to provide important insights into both the magmatic processes involved in crustal accretion and the circulation of seawater-derived hydrothermal fluids through the crust (Morton and

Sleep, 1985; Lister, 1974). On-axis hydrothermal circulation through the sheeted dike complex above the AML extracts heat from the roof of this magma body and drives crystallization within it. What fraction of the lower crustal plutonic rocks crystallize in the AML (losing their latent heat of crystallization into the overlying hydrothermal system) is debated. The gabbro glacier model of crustal accretion (Fig. 1a) suggests the vast majority of the latent heat is lost in this body with crystal subsidence to form the lower crust (Quick and Denlinger, 1993; Henstock et al., 1993; Phipps Morgan and Chen, 1993). The sheeted sill model (Fig. 1b), in contrast, suggests that most of the plutonic section of oceanic crust formed at fast-spreading ridges crystallizes in place (Kelemen et al., 1997; Korenaga and Kelemen, 1997); i.e. the latent heat of crystallization of the plutonic section must be removed from throughout the lower crust. For a given distribution of melt in the lower crust the sheeted sill model thus requires less efficient heat extraction by on-axis hydrothermal circulation above the AML and more efficient off-axis hydrothermal heat extraction from the sides of the LVZ. As a consequence, the different end-member models predict different thermal structures and different variations of cooling rate as a function of depth (Fig. 1). Note that neither of these end-member models, or any hybrid between the two, excludes hydrothermal circulation at any given depth or distance from the ridge axis – the distinction between the models lies in the efficiency (amount and rate) of heat removal by hydrothermal circulation at different locations. Our understanding of crustal accretion mechanisms and the distribution and thermal consequences of hydrothermal fluid flow would be substantially improved by better understanding the thermal structure of the region surrounding the ridge axis.

The temperature structure in the lower oceanic crust at fast-spreading ridges away from the ridge axis is currently poorly constrained. Seismic velocity anomalies at 9°30’N on the East Pacific Rise (EPR), relative to a reference model, were interpreted by Dunn et al (2000) in terms of temperature (and melt fraction) anomalies. This approach led them to suggest that the isotherms in the lower crust are steep, with temperatures <400°C throughout the upper 2 km of the lower crust, within 4 km of the ridge axis. As discussed by Dunn et al. (2000) and Webb (2008), there are considerable uncertainties in the calculation of the thermal structure from seismic velocity variations. For example, close to the ridge, the effect of anelasticity – a relatively poorly known parameter (Dunn et al., 2000) – on seismic wave velocities is prominent. Among other quantities, the activation energy of anelasticity plays a role in the calculations and it is assumed to be the same as the activation energy of creep. Dunn et al. (2000) used a value of 276 kJmol^{-1} (Caristan, 1982) for their inversion of seismic velocities to thermal structure, but subsequently this value has been re-determined to be much higher (~ 485 kJmol^{-1}; Mackwell et al., 1998). As activation energy controls the temperature dependence of properties, a thermal structure calculated using this revised value is likely to be quite different. There are additional sources of uncertainty such as in our knowledge of the power law exponent for the frequency dependence of attenuation and what reference model the seismic structure should be compared to. Notwithstanding such uncertainties, the thermal structure of Dunn et al. (2000) has significantly influenced thinking about processes operating at mid-ocean ridges. For example, this was the starting point for a recent model of hydrothermal circulation developed by Hasenclever et al. (2014). However, compliance data suggest that the crust is partially molten to >5 km off-axis (Crawford and Webb, 2002) in the region studied by Dunn et al. (2000), inconsistent with the thermal structure proposed by Dunn et al. (2000). Likewise, Han et al. (2014) show that at 9°37-40 N on the EPR there are off-axis melt bodies that exist up to 10 km off-axis. Such bodies would rapidly freeze if the off-axis crust was cooled and hence their presence suggests a relatively warm off-axis thermal structure (Han et al., 2014; Coogan, 2014).

The discussion above indicates that there is a need to determine the thermal structure directly, for example by determining cooling rates at different locations. One quantitative approach for determining the thermal structure of the lower crust comes from the petrological tool of *geospeedometry* (Lasaga, 1983). This allows the cooling rate of rocks to be determined from the compositional zoning of minerals. Given a spreading rate, a subsolidus cooling rate can be directly inverted into isotherm separation or compared to cooling rates predicted by thermal models. However, the only attempts to-date to apply such tools to the lower oceanic crust have used the *Ca-in-olivine geospeedometer* (Coogan et al., 2002; Coogan et al., 2007, VanTongeren et al., 2008). Due to paucity of olivine in many evolved gabbros, and the susceptibility of olivine to alteration, this approach has not been widely applied to *in situ* crust formed at fast-spreading ridges. Here, we apply a new approach specifically developed to be suited to such rocks.

Clinopyroxene and plagioclase are virtually omnipresent in the lower oceanic crust and thus a geospeedometric method based on exchange of Mg between these phases was developed (Faak et al., 2014). Natural rock samples from the oceanic crust show much higher concentrations of MgO in plagioclase phenocrysts in mid ocean ridge basalts (MORBs) than in the cogenetic, but more slowly cooled, gabbroic rocks of the lower oceanic crust (Fig. 13f in Coogan, 2014). This difference in plagioclase Mg-content is explained by diffusion out of the plagioclase into the clinopyroxene during cooling. The partition coefficient of Mg between plagioclase and clinopyroxene, $K_{Mg}^{Pl/Cp}$, decreases with temperature (Faak et al., 2013), i.e., during cooling an exchange of Mg between plagioclase and clinopyroxene rims is required for these to remain in equilibrium. The exchange process leads to the development of a Mg concentration gradient within the plagioclase as Mg diffuses out of plagioclase and into clinopyroxene. Diffusion is a thermally activated process and becomes slower with decreasing temperatures. Hence, there will be a temperature, Tc, at which diffusion becomes too slow for measurable Mg loss from the plagioclase. This closure temperature (Tc) depends on the distance from the interface (Dodson, 1986; Onorato et al., 1981), such that the rims of a plagioclase crystal will be able to maintain equilibrium Mg-concentrations down to lower temperatures than the core of the crystal, leading to the development of a closure profile that is convex upwards for a continuous cooling history. Faak et al. (2014) show how the evolution of the resulting concentration profile of Mg in plagioclase depends on the cooling history. For example, a slow cooling rate will allow extensive diffusive exchange of Mg from plagioclase into clinopyroxene leading to low Mg contents of plagioclase. In contrast, fast cooling rates will lead to high plagioclase Mg contents if all other relevant parameters (grain size, grain shape, anorthite content) remain unchanged (for a detailed discussion on the evolution of diffusion profiles for different cooling histories and additional factors influencing the resulting shape of the profile see Faak et al., 2014). Here we apply the *Mg-in-plagioclase geospeedometer* (Faak et al., 2014) to three suites of oceanic gabbros that formed at the East Pacific Rise to determine their cooling history and infer the thermal state of the ridge axis region.

2. The Sample Suites

There are only three locations in the world where well-located samples of the upper plutonic section of oceanic crust formed at modern fast-spreading ridges have been collected. These are the *Hess Deep Rift* in the equatorial Pacific, the *Pito Deep* in the southern Pacific, and *IODP (International Ocean Discovery Program) Site 1256D* in the eastern Pacific (Fig. 2a). For this study we investigated samples from all three locations and from different depths within the lower oceanic crust.

The largest and best constrained sample suite is from the *Hess Deep Rift*, where ~1 Ma old crust that formed at the equatorial East Pacific Rise (full spreading rate ~135 mmy^{-1}), is rifted apart due to the westward propagation of the Cocos-Nazca spreading center (Lonsdale, 1988; Francheteau et al., 1990). The rifting has created a tectonic window (Fig. 2b) that exposes the entire upper crust (lavas and dikes, ~1200 m) as well as the upper part (~1000 m) of the gabbros (Karson et al., 2002). This study mainly focuses on samples collected by submersible from the North wall of the Hess Deep Rift (Lonsdale, 1988; Karson et al., 2002, Fig. 2d and e). Because the dike/gabbro boundary (DGB) was mapped on multiple dives (Figure 2d), and the depth below sea level is known for each sample, it is possible to reconstruct the depth below the DGB for each sample (Table 1).

The second sample suite comes from *Pito Deep*, where ~3 Ma old crust formed at the EPR (full spreading rate ~140 mmy^{-1}) is rifted apart due to a propagating rift tip at the northeastern corner of the Easter Microplate (Francheteau et al., 1988; Hey, 1995, Fig. 2c). Continuous sections of the oceanic crust including lavas, sheeted dikes and the upper gabbroic rocks are exposed (Constantin et al., 1995; Hekinian et al., 1996, Constantin et al., 1996; Perk et al., 2007). Gabbroic rocks investigated in this study were collected during the *Jason II* and *Alvin* dive programs during cruise AT11-33 of the R/V *Atlantis* (e.g., Perk et al., 2007; Figure 2f and g), The DGB was mapped during the dives (Figure 2f), which allows us to reconstruct the depth below the DGB for each sample (Table 1).

The final place that a short section of plutonic rocks formed at a modern fast-spreading ridge have been sampled at is *IODP Site 1256D,* which drilled into ~15 Ma old intact oceanic crust of the Cocos Plate that formed at the superfast spreading EPR (full spreading rate ~220 mmy^{-1}). In this drilling project ~1250 m of oceanic crust has been sampled to-date, providing a section from extrusive lavas, through sheeted dikes and into the top of the plutonic section (Wilson et al., 2006). Hole 1256D penetrated the top of the plutonic section where gabbros and granoblastic dikes are intermixed (Wilson et al., 2006; Koepke et al., 2008; France et al., 2009; Sano et al., 2011).

3. Mg-concentration profiles in plagioclase

In order to apply the *Mg-in-plagioclase geospeedometer* to the most suitable rocks from these sample suites, gabbroic rocks with coexisting plagioclase and clinopyroxene that appear fresh (i.e. nearly unaltered) were chosen. In addition, plagioclase crystals with nearly idiomorphic grain shapes and high aspect ratios were selected, and a full profile (rim-core-rim) was measured along the short dimension of the crystal to minimize effects from diffusion in three dimensions (Faak et al., 2014). The composition of the clinopyroxene adjacent to each profile was analyzed when possible. If no clinopyroxene was directly adjacent to a profile, then a clinopyroxene in close proximity to the respective plagioclase was analyzed. Some Mg-profiles were measured along a profile, where plagioclase was in direct contact with clinopyroxene on one side, but with another plagioclase crystal on the other side (but with clinopyroxene in close proximity) to test if grain boundaries acted as fast pathways for diffusion. If they did then plagioclase is expected to exchange Mg with a neighboring clinopyroxene, even when the grains are not in direct contact, and the measured Mg-profile should show approximately the same Mg-concentration on both rims (for similar X_{An} on both rims; see Dohmen and Chakraborty, 2003 for a quantitative explanation). As discussed below this allows us to evaluate whether transport along the grain boundary is infinitely fast and efficient or if transport along grain boundaries limits Mg exchange between plagioclase and clinopyroxene grains if they are separated by too long a distance.

3.1 Measurement of Mg-concentration profiles in plagioclase

The concentration of Mg and major elements in plagioclase was measured using a *Cameca SX-50* electron microprobe (EMP) fitted with four wavelength-dispersive spectrometers at the Ruhr-Universitaet in Bochum. Natural and synthetic mineral standards were used for calibration and an on-line φ(ρz)/PAP correction procedure was used to correct for absorption, fluorescence and atomic number. To attain high precision analysis of Mg in plagioclase, the measurement conditions outlined by Faak et al. (2014) were applied (also see Supplemental Table S1 for details). Briefly, these are: beam current = 40 nA, accelerating voltage = 15 kV, and long counting times for Mg (90 s on the peak and 45 s on each background, with the background positions selected specifically for the measurement of Mg in plagioclase), which allows a 3σ detection limit of ~75 ppm to be achieved. Using these conditions the precision on Mg in plagioclase at a concentration of 0.05 wt% MgO is ~0.0025 wt% on this instrument. The distance between analyzed spots along the profile was 5 μm for shorter profiles and 10 μm for longer profiles. The first and last measurements at the rims of the plagioclase were approximately 2 to 5 µm away from the interface.

3.2 Mg-concentrations and profile shapes as function of depth in the plutonics

The measured concentrations of MgO in plagioclase from all sample suites vary between 0.01 wt% (at some of the rims) and 0.13 wt% (at the cores of the shallowest samples). In the same plagioclase grain, Mg-concentrations at the rim are similar for plagioclase-clinopyroxene contacts and plagioclase-plagioclase contacts, implying that the grain boundaries indeed act as fast pathways for the Mg-exchange (see above).

Samples from the Hess Deep and Pito Deep sample suites studied here, cover a depth range from 0 to 520 m and 42 to 836 m below the DGB, respectively, and allow variation of the plagioclase Mg-concentration profiles as a function of depth to be observed. Both sample suites show a systematic decrease of MgO in the cores of plagioclase crystals with increasing sample depth (Fig. 3). The plagioclase rims show MgO-concentrations between 0.01 to 0.05 wt%, with no systematic variation with the sampling depth. This leads to Mg-profiles with stronger curvature in the shallower samples (i.e., larger difference in Mg content between the cores and rims, e.g., Fig. 3a and e) and rather homogeneous Mg-profiles for the deeper samples (i.e., equally low Mg-concentrations at the core and the rims, e.g., Fig. 3d and h).

Many samples from the IODP Site 1256D show MgO-concentrations below the detection limit of the EMP, and the plagioclase appears to be hydrothermally altered – we interpret this as indicating that Mg-loss occurred during dissolution-reprecipitation reactions rather than via solid-state diffusion. Only two shallow samples (12.1 and 12.4 m below the DGB) from this location were suitable for modeling using the approach of this study (Table 1).

4. Modeling diffusion profiles of Mg in plagioclase and fitting the natural data

4.1 Diffusion model and parameters

Cooling rates are obtained from diffusion modeling of Mg in plagioclase, using the *Mg-in-plagioclase geospeedometer* of Faak et al. (2014). This method is based on the diffusive exchange of Mg between plagioclase and clinopyroxene under the assumptions of: (i) instantaneous equilibrium at the interface between the two phases, and (ii) clinopyroxene acting as an infinite reservoir. As described above (Section 1), during cooling, the Mg-concentration at the interface changes, and the resulting concentration gradient provides a driving force for diffusion out of the plagioclase into the clinopyroxene. As diffusion of Mg in plagioclase is coupled with the anorthite content, X_{An}, in plagioclase, this has to be accounted for in the diffusion equation (Costa et al., 2003; Appendix A). Additionally, the diffusion coefficient of Mg in plagioclase, D_{Mg}^{Pl}, and the partition coefficient $K_{Mg}^{Pl/Cpx}$ depend on the silica activity, a_{SiO_2}, of the system (Faak et al., 2013; Appendix A), which therefore needs to be constrained.

Faak et al. (2014) show how the general *Mg-in-plagioclase geospeedometer* may be specifically applied to rocks from the lower oceanic crust, and here we follow the approach outlined in their example. In detail, (i) the diffusion coefficient D_{Mg}^{Pl} and the partition coefficient $K_{Mg}^{Pl/Cpx}$ are taken from Faak et al. (2013), as those were specifically determined in the compositional range of plagioclase and clinopyroxene found in the lower oceanic crust; (ii) an initial profile for Mg in plagioclase is calculated from $K_{Mg}^{Pl/Cpx}$ at temperatures around 1200°C, where the exact starting temperature, T_{start}, depends on the grain size of the plagioclase; (iii) the silica activity, a_{SiO_2}, is assumed to be constrained by the assemblage olivine + orthopyroxene (Appendix A), since this assemblage is found in many of the samples investigated here (see Faak et al., 2014 for details and discussion). The change in plagioclase Mg-concentration due to diffusion is calculated iteratively along a given cooling path using a finite difference approach (Faak et al., 2014; Appendix A). As a first approximation, a linear cooling path over the modeled temperature interval is assumed, and the cooling rate dT/dt is iteratively refined until the best visual match between the measured and the modeled Mg-profile is found.

4.2 The temperature interval

Under the assumption of instantaneous equilibrium at the interface between plagioclase and clinopyroxene, diffusion along a linear cooling path produces Mg-closure-profiles that are convex upwards (Faak et al., 2014), i.e., have lower Mg-concentrations at the rims than at the core. The measured Mg-concentration profiles from the oceanic crust commonly show a significantly smaller degree of convex curvature, than would be expected from the model of Faak et al. (2014) for a cooling history in which temperature changes as a linear function of time (i.e., a constant cooling rate). The lack of a strong curvature of the Mg-profiles can be explained in two ways, either: (A) the approximation of a linear cooling history is only valid up to a certain temperature, and the cooling rate increases below this temperature. A cooling history with increasing cooling rates towards lower temperatures produces more homogeneous Mg-profiles (Faak et al, 2014); or, (B) the assumption of instantaneous equilibration at the crystal interface is only valid above a certain temperature (here referred to as T_{closed}). This means, Mg is not effectively exchanged between plagioclase and clinopyroxene below T_{closed}; however, diffusion of Mg in plagioclase continues in a closed system and tends to homogenize the Mg-concentration (for a homogeneous X_{An}-content), leading to less curvature in the measured Mg-profile (for details see Appendix B). Faak et al. (2014) briefly discuss this issue and model two examples from the oceanic crust. They defined a temperature, Tc_{rim}, that is calculated from the measured Mg-concentration at the rim (defined as 2-5 µm from the interface) of a plagioclase crystal with a clinopyroxene (Faak et al., 2014). This temperature is interpreted as the closure temperature below which diffusion ceased to change the Mg-concentration significantly in a region 5 µm away from the interface. Hence, Faak et al. (2014) end the modeling procedure for a linear cooling rate at this temperature Tc_{rim}, implying that diffusion effectively stops below this temperature (i.e., they model scenario (A)). They show that it is possible to fit strongly curved and homogeneous Mg-profiles using this approach.

For this study, we also investigated the evolution of diffusion profiles of Mg in plagioclase for the case of exchange of Mg between plagioclase and clinopyroxene ceasing below a temperature T_{closed}, and the continuation of Mg diffusion in plagioclase in a closed system (i.e., scenario (B), see Appendix B). In this model the bulk Mg content of the plagioclase does not change below T_{closed} and the diffusive fluxes within the plagioclase below this temperature have to be sufficient to homogenize the Mg-distribution. These combined constraints tightly constrain the maximum cooling rates. Both modeling approaches were applied to three hypothetical plagioclase crystals (P1: weakly curved Mg-profile with 0.04 wt% MgO at the rims and 0.06 wt% MgO at the core; P2: homogeneous Mg-profile at 0.04 wt% MgO; P3:

homogeneous Mg-profile at 0.02 wt% MgO; all with homogeneous $X_{An} = 0.6$). The direct comparison of the two scenarios for identical plagioclase crystals shows that T_{closed} is always slightly lower than Tc_{rim} (25°C for P1, and 20°C for P2 and P3; Appendix B). The cooling rates dT/dt determined for the temperature interval above T_{closed} are slightly faster, when scenario B is modeled (e.g., P1: dT/dt = 0.008°Cy^{-1} for scenario (A) and 0.01°Cy^{-1} for scenario (B); P2: dT/dt = 0.0003°Cy^{-1} for scenario (A) and 0.001°Cy^{-1} for scenario (B); Appendix B). Thus, for homogeneous Mg-profiles, the levels of variation in dT/dt and Tc_{rim} / T_{closed} arising from the choice of the modeling approach (A vs. B) are in the range of other uncertainties of the *Mg-in-plagioclase geospeedometer* (e.g., uncertainties in cooling rate arising from the choice of D_{Mg}^{Pl} can lead to a factor of 3 difference in cooling rate; Faak et al., 2014). For Mg-profiles with some degree of curvature, the differences are even smaller. The cooling rates presented below were determined using method A.

5. Cooling rates as a function of depth in the plutonic section of EPR crust

Cooling rates were obtained from 41 individual plagioclase crystals (51 profiles) in 23 samples from the three sample suites (32 profiles in 13 samples from Hess Deep, 16 profiles in 8 samples from Pito Deep, 3 profiles in 2 samples from IODP Site 1256D; Table 1; Supplemental Material), spanning a total depth interval below the DGB of 0 to 836 m. Cooling rates systematically decrease with increasing depth, and cover almost 4 orders of magnitude, ranging from ~1 °Cy^{-1} for the shallowest samples to 0.0003°Cy^{-1} for the deepest samples (Table 1, Fig. 4). Cooling rates from all three sample suites agree very well with each other (with respect to their individual depth below the DGB) and fall on the same trend (Fig. 4).

The uncertainty for each data point (i.e. the uncertainty of the cooling rate obtained from each Mg-profile) cannot be expressed by a simple analytical expression for propagation of errors. This is because, in addition to uncertainties arising from the error associated with each individual parameter in the diffusion equation, the overall uncertainty in the determination of cooling rates also depends on factors such as the X_{An}-gradient in the plagioclase crystal. However, Faak et al. (2014) evaluated the overall uncertainty in the procedure using Monte-Carlo simulations and simulated profiles with unzoned X_{An} and known thermal histories. They also evaluated the uncertainty that results from the use of different sets of diffusion coefficients (i.e. Van Orman et al., 2014 and Faak et al., 2013). They found that cooling rates can be determined to better than half an order of magnitude. Additionally, the difference in the obtained cooling rates from multiple Mg-profiles in multiple plagioclase crystals in the same sample (i.e. the scatter in the data for one sample) may be taken as a measure for the precision of the cooling rate estimate for a single sample. Following this approach, the precision on the obtained cooling rate is also found to be better than half an order of magnitude. therefore, the uncertainties are much smaller than the observed decrease in cooling rate of almost four orders of magnitude.

The cooling rates obtained here are similar to those derived from a small subset of the samples using *Ca-in-olivine geospeedometry* (Coogan et al., 2007) and from a larger sample suite from the Oman ophiolite (Fig. 4). The fact that two different methods (*Mg-in-plagioclase* and *Ca-in-olivine*), which are based on different diffusion and partition coefficients, yield similar values for the cooling rate at a given depth below the DGB implies that not only is the relative variation in cooling rate with depth well constrained, but also that the absolute values of cooling rates are robust (i.e., the cooling rates are accurate as well as precise). Importantly, the very similar cooling rates extracted from four different crustal sections indicates that cooling rates in the uppermost plutonics formed at fast-spreading ridges are similar – i.e., the thermal structure must be similar and close to steady-state. We expand on these points below.

One sample from the Pito Deep suite yields cooling rates that are shifted from the cooling rate versus depth trend defined by all the other samples to slower cooling rates (sample 022005-1052, Table 1 and Fig. 4). The slow cooling rates obtained from this sample are due to the low Mg-content (~0.015-0.03 wt% MgO) of plagioclase in this sample. We do not have any explanation for this observation at this point of time and treat this as an outlier from the general trend.

6. Discussion - implications for the mode of cooling of the oceanic crust and comparison to thermal models

The observed variation in cooling rate with depth is very consistent for three different sections of crust formed at the EPR (and the Oman ophiolite; Fig. 4), implying a similar thermal structure in the near-axis region along the EPR. This indicates that the thermal structure is near steady-state in the temperature window recorded (~1100-700°C; Table 1). The significant decrease of cooling rate with increasing depth in the uppermost part of the oceanic lower crust (~4 orders of magnitude over 840 m below DGB) provides a fundamental constraint on models of crustal accretion and hydrothermal circulation at fast-spreading ridges.

The cooling rates determined here are compared to those from modeling studies, and the inversion of seismic velocity into temperature, in Fig. 5. Both the absolute cooling rates determined from the deeper samples (>300 m below DGB) and the large decrease in cooling rate with depth are inconsistent with thermal models that include substantial cooling by off-axis hydrothermal circulation. For example, Maclennan et al. (2005) report the results of three thermal models that have 50-71 kWm^{-1} of hydrothermal cooling off-axis. These models calculate little variation in cooling rate with depth, faster cooling rates than those observed (except in the upper ~100 m; blue lines in Fig. 5), and are inconsistent with the depth distribution of cooling rates determined by geospeedometry. The same is true of the more sophisticated thermal model of Hasenclever et al. (2014) and the cooling rates predicted by the isotherm separation of Dunn et al. (2000) that this model is based on (blue crosses in Fig. 5).

While the cooling rates determined here are inconsistent with models with extensive off-axis hydrothermal heat extraction at depth (Maclennan et al., 2005; Hasenclever et al., 2014; blue area in Fig. 5), they are broadly consistent with conductive cooling models (green lines in Fig. 5). This does not mean that there is no hydrothermal circulation in this region, or that it extracts no heat from the lower crust, but just that the thermal effects of such circulation are minor. Near conductive cooling rates in the upper part of the lower oceanic crust are consistent with the recent finding of off-axis sills in the lower crust along the East Pacific Rise (Canales et al., 2009; Han et al., 2014). The recent discovery of on-axis, sub-axial melt lenses (Marjanovic et al., 2014) provides no new constraints on the thermal structure of the axial region because it has long been thought that this region contains partial melt due to the low seismic velocities (e.g. Harding et al., 1989). If the crust was efficiently cooled in the off-axis by hydrothermal circulation, producing the kind of thermal structure suggested by Dunn et al. (2000) and Hasenclever et al. (2014), then any magma intruded off-axis would be emplaced into cold wall-rocks and hence would freeze rapidly. For example, using Eq. (3) in Chapter 2.2 in Carslaw and Jaeger (1959), a 200 m high sill that intruded at 1200°C into country rock with a temperature of 600°C would solidify within <1000 y even if conduction was the only heat transport mechanism; since extensive hydrothermal circulation is required for the off-axis region to be cool, this calculation over estimates the solidification time. Hence the probability of observing such bodies in seismic studies would be very small (Coogan, 2014; Han et al., 2014). In contrast, the near conductive cooling rates determined here imply warm off-axis upper plutonic crust, and hence longer off-axis sill lifetimes, and a higher probability of identifying these bodies seismically.

The observed plagioclase Mg contents, the shapes of their Mg zoning profiles, and their variation with depth provide information about: (a) the temperatures around which exchange of Mg with surrounding clinopyroxene froze (~ Tc_{rim} in our notation), and (b) the cooling rates around these temperatures as a function of depth. These allow us to constrain the earliest point of time (equivalent to distance from the axis in a ridge-spreading situation with a known spreading-rate) at which the temperature Tc_{rim} may have been reached at a given depth (Fig. 6). This is obtained by assuming the physically unrealistic, but mathematically limiting, case where cooling above (Tc_{rim} + 100 °C) was instantaneous. Any other more physically realistic cooling scenario would lead to the observed Tc_{rim} at that depth being attained at a later point of time and hence greater distance from the ridge (marked as gray field in Fig. 6). This information extracted from the compositional characteristics (concentration, zoning pattern) of plagioclase crystals may be compared with those obtained from studies where the thermal structure was obtained by thermal modeling or inverting other kinds of data such as seismic velocity profiles (e.g., Hasenclever et al., 2014; Dunn et al., 2000). As seen in Fig. 6, these predict much lower temperatures (~ 400

°C) at depths greater than 500 m below the dike / gabbro boundary at much earlier times, and hence much closer to the ridge axis (due to the much faster cooling rates in Fig. 5). These trends fall well outside the gray region in Fig. 6 that is permissible based on the observations of the compositional characteristics of plagioclase. In other words, the thermal structure of the upper part of the lower crust that we obtain from our observations is inconsistent with the models of Hasenclever et al. (2014) or Dunn et al. (2000).

We have discussed above (Section 1) how the inversion of seismic velocity perturbations to yield thermal anomalies may be affected by uncertainties in our knowledge of several material parameters. The hydrothermal circulation model of Hasenclever et al. (2014) is anchored to the model of Dunn et al. (2000) and is subject to the same sources of uncertainty. Additionally, in spite of the sophistication of their calculations, there are aspects that could be improved – for example, consideration of anisotropy of permeability and distinct permeabilities for gabbros and sheeted dike complexes may yield more realistic hydrothermal circulation patterns. Therefore, the mismatch between the results from these models and the directly determined cooling rates of this study is not surprising. Indeed, the direct determination of the spatial distribution of cooling rates as a function of depth in this study provides important boundary conditions that may be used to develop the next generation of such models.

7. Summary and conclusions

A new geospeedometer, based on the Mg content of plagioclase co-existing with clinopyroxene, was applied to natural gabbroic rocks from three locations where samples of the plutonic section of oceanic crust formed at modern fast-spreading ridges are available. Samples from each location originate from different depths below the DGB and the total depth interval covers the upper 836 m of the plutonic section of the oceanic crust. The obtained cooling rates decrease significantly with increasing sample depth (covering almost 4 orders of magnitude, ranging from ~1 °Cy^{-1} for the shallowest samples to 0.0003°Cy^{-1} for the deepest samples). The fact that this observation is very robust for three different locations along the EPR implies a very comparable, and near steady-state, thermal structure in the off-axis region along the EPR. Two independent methods (*Mg-in-Pl* and *Ca-in-Ol*) give the same cooling rates for a given depth below the DGB, which implies that not only is the relative trend of cooling rate with depth well constrained, but also that the absolute values obtained for the cooling rates are robust. Both, the absolute cooling rates determined from the deeper samples (>300 m below DGB), and the large decrease in cooling rate with depth, are inconsistent with thermal models that include substantial cooling by off-axis hydrothermal circulation. Instead, our data is consistent with thermal models in which the lower crust cools conductively in the off-axis, implying that most of the latent heat is removed by hydrothermal circulation at the top of an axial melt lens and heat conduction becomes the dominant process of heat removal with increasing depth and away from the ridge axis. Our observational results provide important additional boundary conditions for modeling calculations of thermal structure of fast spreading ridge systems (e.g., Maclennan et al., 2005; Hasenclever et al., 2014), and should help in the development of the next generation of models.

8. Acknowledgements

We would like to thank Jeff Karson, Kathryn Gillis and IODP for the generous loan of samples. Stan Dosso is thanked for helping to speed up the Fortran code for the forward model and providing an inversion method to test the forward model. We thank an anonymous reviewer and the editor Tim Elliot for constructive reviews and comments that helped to improve the clarity of the paper and acknowledge support from DFG SC 166/12-1 and NSERC discovery grant 283238.

Appendix A Model parameters and input conditions for the diffusion model

A detailed description of the used diffusion model may be found in Faak et al. (2014), here we briefly summarize the modeling approach and the input parameters used.

Diffusion equation and diffusion coefficient

The diffusion of Mg in plagioclase is coupled with the anorthite content, X_{An}, in plagioclase, which needs to be accounted for in the diffusion equation (Eq. (7) in Costa et al., (2003)):

$$J_{Mg} = D_{Mg}\frac{\partial C_{Mg}}{\partial x} + L_{Mg}A\frac{\partial X_{An}}{\partial x} \qquad \text{(Eq. A.1)}$$

where D_{Mg} = diffusion coefficient of Mg in plagioclase, C_{Mg} = concentration of Mg in plagioclase, x = distance and A = factor to describe the dependence of the partition coefficient on X_{An}. Their factor L_{Mg} is a phenomenological coefficient, equivalent to $(D_{Mg}C_{Mg})/RT$ (see Costa et al. (2003) for details). The resulting diffusion equation to describe the flux of Mg has been presented by Costa et al. (2003):

$$\frac{\partial C_{Mg}}{\partial t} = \left(D_{Mg}\frac{\partial^2 C_{Mg}}{\partial x^2} + \frac{\partial C_{Mg}}{\partial x}\frac{\partial D_{Mg}}{\partial x}\right) - \frac{A}{RT}\left(D_{Mg}\frac{\partial C_{Mg}}{\partial x}\frac{\partial X_{An}}{\partial x} + C_{Mg}\frac{\partial D_{Mg}}{\partial x}\frac{\partial X_{An}}{\partial x} + D_{Mg}C_{Mg}\frac{\partial^2 X_{An}}{\partial x^2}\right) \qquad \text{(Eq. A.2)}$$

where t = time.

The differential equation (Eq. (A.2)) can be solved numerically for one-dimensional diffusion in a plate by applying the method of central finite differences (Crank, 1975, Costa et al., 2008):

$$C_{i,j+1} = C_{i,j} + \frac{\Delta t}{\left(2\Delta x^2\right)}\left[D_{i,j}\left(C_{i+1,j} - 2C_{i,j} + C_{i-1,j}\right) + \frac{1}{2}\left(C_{i+1,j} - C_{i-1,j}\right)\left(D_{i+1,j} - D_{i-1,j}\right)\right]$$

$$-\frac{A}{RT}\frac{\Delta t}{\left(2\Delta x^2\right)}\begin{bmatrix} \frac{1}{2}D_{i,j}\left(C_{i+1,j} - C_{i-1,j}\right)\left(X_{An_{i+1,j}} - X_{An_{i-1,j}}\right) \\ +\frac{1}{2}C_{i,j}\left(D_{i+1,j} - D_{i-1,j}\right)\left(X_{An_{i+1,j}} - X_{An_{i-1,j}}\right) \\ +D_{i,j}C_{i,j}\left(X_{An_{i+1,j}} - 2X_{An_{i,j}} + X_{An_{i-1,j}}\right) \end{bmatrix}$$

(Eq. A.3)

where i = step in distance and j = step in time. $C_{i,j}$ and $D_{i,j}$ are the concentration of Mg in plagioclase and the diffusion coefficient of Mg in plagioclase at given i and j, respectively.

We used the diffusion coefficient of Mg in plagioclase from Faak et al. (2013) that was determined experimentally in the compositional range of the lower oceanic crust:

$$D_{Mg}^{Pl}\left[\mathrm{m^2 s^{-1}}\right] = 1.25 \cdot 10^{-4}\ \left[\mathrm{m^2 s^{-1}}\right] \cdot \exp\left(-320924\left[\mathrm{J\,mol^{-1}}\right]/(RT)\right)\left(a_{SiO_2}\right)^{2.6}.$$

(Eq. A.4)

Initial and boundary conditions

The partition coefficient, $K_{Mg}^{Pl/Cpx}$, has been determined experimentally by Faak et al. (2013) and is given by the relationship:

$$\ln K_{Mg}^{Pl/Cpx} = -9219\left[K\right]\frac{1}{T} + 1.6 + \frac{16913\left[J mol^{-1}\right]}{RT}X_{An} + \ln a_{SiO_2}$$ (Eq. A.5)

This can be re-arranged to give the interface plagioclase composition as a function of the measured clinopyroxene composition, temperature and the silica activity in the system:

$$C_{Mg}^{Pl} = C_{Mg}^{Cpx} \exp\left[-9219[K]\frac{1}{T} + 1.6 + \frac{16913[Jmol^{-1}]}{RT} X_{An} + \ln a_{SiO_2} \right] \quad \text{(Eq. A.6)}$$

An initial profile is calculated based on Eq. (A.5) at temperatures around 1200°C, (the exact starting temperature T_{start} depends on the grain size of the plagioclase and is given in Table 1).

Silica activity

Solving equations (A.4-A.6) requires knowledge of the silica activity, a_{SiO_2}, as a function of temperature. Here, we assume a_{SiO_2} is constrained by the assemblage olivine + orthopyroxene as these are commonly observed phases in the samples studied. Thus, a_{SiO_2} is given by the reaction:

$$Mg_2SiO_4 + SiO_2 = 2MgSiO_3 \quad \text{(Eq. A.7)}$$

and the relationship proposed by Carmichael et al. (1970):

$$\log a_{SiO_2} = \frac{\Delta G_r}{2.303RT} \quad \text{(Eq. A.8)}$$

where ΔG_r is the Gibbs Free energy of the reaction given in equation (A.7). The silica activity defined by Eq (A.7) at 1 bar was calculated for pure Mg-endmembers (Faak et al., 2013 report that the incorporation of a molar fraction of 0.1 of the respective Fe-endmembers increases a_{Si_2O} by about 10%) and for different temperatures using the data set of Ghiorso and Sack (1995) to determine ΔG_r, and the resulting dataset fitted by a 2nd-order polynomial to obtain:

$$a_{SiO_2} = -4.86904\,10^{-7}\,T^2 + 1.51570\cdot10^{-3}\,T - 0.61870 \qquad \text{(Eq. A.9)}$$

Appendix B

Section 4.2 discusses how the lack of a strong curvature of the Mg-profiles and the high Mg-concentrations at the rims, which is measured in plagioclase from the lower oceanic crust, can be explained by two possible scenarios. This Appendix illustrates the modeling approaches used to simulate these different scenarios, and shows that this leads to only small differences in the extracted cooling rates.

We consider two scenarios. Scenario (A) assumes a linear cooling history up to a certain temperature, Tc_{rim}, which can be calculated from the measured Mg-concentration at the rim of a plagioclase crystal (Eq. (4) in Faak et al., 2014). Below Tc_{rim} cooling continues with an increased cooling rate, fast enough such that the diffusion profile, which was evolved up to Tc_{rim}, is not significantly modified.

Scenario (B) assumes a cooling history that is linear down to temperatures low enough that the diffusion profile is not effectively changed by diffusion anymore (around 600°C for the diffusion of Mg in plagioclase and geological reasonable cooling rates). However, in this scenario there is a certain temperature T_{closed} (>600°C) below which the exchange of Mg between plagioclase and clinopyroxene ceases. However, diffusion of Mg within the plagioclase continues and tends to homogenize the concentration of Mg in plagioclase (or for plagioclase zoned in X_{An}, tends to equilibrate the plagioclase Mg content with the An content). Thus, in model B, the system continues cooling down to 600°C at the same cooling rate, but diffusion of Mg below T_{closed} is simulated in a closed system (= plagioclase has closed boundary conditions). An additional constraint on this scenario comes from the argument of mass balance: if Mg cannot be exchanged below T_{closed}, the total amount of Mg in plagioclase at this temperature (Mg_{tot}) *must* equal the final amount of Mg in plagioclase, $Mg_{observed}$. Since we model diffusion in 1D, assuming a plane sheet geometry, the amount of Mg in plagioclase is calculated along a Mg-profile as $Mg = Mg(x)*dx$, where $Mg(x)$ is the concentration of MgO in wt% at a certain grid point and dx is the distance between grid points. We define that mass balance is fulfilled if $Mg_{tot} = Mg_{observed} \pm 1\%$.

The two different approaches were applied to three theoretical plagioclase crystals: P1 has a weekly curved Mg-profile with 0.04 wt% MgO at the rims and 0.06 wt% MgO at the core (Fig. B1 a-c); P2 has a homogeneous Mg-profile at 0.04 wt% MgO (Fig. B1 d-e) and P3 has a homogeneous Mg-profile at 0.02 wt% MgO (Fig. B1 g-i). When modeled as scenario (A), the best fit between modeled and observed data is obtained for the following values: dT/dt=0.008°Cy^{-1} and Tc_{rim} = 910°C for P1 (Fig. B1a), dT/dt = 0.0003°Cy^{-1} and Tc_{rim} = 910°C for P2 (Fig. B1d), and dT/dt = 0.00002°Cy^{-1} and Tc_{rim} = 810°C for P2 (Fig. B1g). Note that for P2 and P3, where the observed Mg-profiles are homogeneous, only maximum cooling rates can be obtained. For homogeneous X_{An}, these homogeneous Mg-profiles represent the equilibrium Mg-concentration at Tc_{rim} and would not be changed by slower cooling. When modeling scenario (B), once a cooling rate for a model run is fixed, there is only limited variation for T_{closed}, i.e. for a given cooling rate, T_{closed} can only be changed by a few °C without violating the mass balance criteria (in fact, if Mg_{tot} exactly equals $Mg_{observed}$, then T_{closed} is fixed for a given cooling rate). Furthermore, diffusion below T_{closed} will tend to homogenize the Mg-profile, i.e. decrease the Mg-concentration at the core and increase the Mg-concentration at the rims. Thus, mass balance can only be fulfilled if T_{closed} is lower than Tc_{rim} and dT/dt is faster than dT/dt in scenario (A). However, if dT/dt is too fast, mass balance cannot be attained for any temperature T_{closed}, because Mg is not removed efficiently enough from the core. Even for cases where mass balance can be attained, dT/dt may be too fast to allow for sufficiently diffusion of Mg in the closed system to allow a good match between the observed and the modeled profile (e.g. Fig. B1 c, f, and i). In the end, there is only a small range of combinations of dT/dt and T_{closed} that lead to acceptable fits to the observed Mg-profiles (e.g. Fig. B1 b, e, and h).

To obtain an estimate of the level of variation of dT/dt and Tc_{rim} / T_{closed} that is introduced by the choice of modeled scenario, we used dT/dt and Tc_{rim} from modeling scenario (A) (Fig. B1 a, d, and g) as a starting point for modeling scenario (B). Then dT/dt was iteratively increased, and T_{closed} was adjusted for each run until mass balance was fulfilled. For each plagioclase, the last fit that was still considered 'acceptable' is shown in Fig. B1 b, e, and h. The next run with fits that were not accepted any more is shown in Fig. B1 c, f and i. The difference between dT/dt and Tc_{rim} / T_{closed} from scenario (A) and those obtained from last accepted fit from scenario (B) show the small difference in cooling rate extracted using these different approaches as discussed in the main text.

References

Canales, J. P., Nedimovic, M. R., Kent, G. M., Carbotte, S. M., Detrick, R. S., 2009. Seismic reflection images of a near-axis melt sill within the lower crust at the Juan de Fuca ridge. Nature, 460, 89-93.

Caristan, Y., 1982. The transition from high temperature creep to fracture in Maryland diabase. J. Geophys. Res., 87, 6781-6790.

Carmichael, I. S. E., Nicholls, J., and Smith, A. L., 1970. Silica activity in igneous rocks. *Am. Mineral.* **55**, 246-263.

Carslaw, H. S., Jaeger, J. C. 1959. *Conduction of heat in solids*. Oxford University Press. Oxford.

Constantin, M., Hekinian, R., Ackermand, D., Stoffers, P., 1995. Mafic and ultramafic intrusions in upper mantle peridotties from fast spreading centers of the Easter Microplate (South East Pacific). in: Vissers, R. L. M., Nicolas, A. (Eds.) Mantle and Lower Crustal Exsposures in Ocean Ridges and in Ophiolites, pp. 71-120, Kluwer Academic, Dortrecht.

Constantin, M., Hekinian, R., Bideau, D., Hébert, R., 1996. Construction of the oceanic lithosphere by magmatic intrusions: Petrological evidence from plutonic rocks formed along the fast-spreading East Pacific Rise. Geology, 24, 731-734.

Coogan, L. A., Jenkin, G. R. T., Wilson, R. N., 2002. Constraining the cooling rate of the lower oceanic crust: a new approach applied to the Oman ophiolite. Earth Planet. Sci. Lett., 199, 127-146.

Coogan, L. A., Jenkin, G. R. T., Wilson, R. N., 2007. Contrasting cooling rates in the oceanic lithosphere at fast- and slow-spreading mid-ocean ridges derived from geospeedometry. J. Petrol., 48, 2211-2231.

Coogan, L. A., 2014. The lower oceanic crust. in: Turekian, K., Holland, H. D (Eds.) Treatise on Geochemistry: The Crust (Vol. 4), pp. 497-541, Elsevier, New York.

Costa, F., Chakraborty, S., Dohmen, R., 2003. Diffusion coupling between major and trace elements and a model for the calculation of magma chamber residence times using plagioclase. Geochim. Cosmochim. Acta, 67, 2189-2200.

Crank, J., 1975. *The mathematics of diffusion*. Oxford Scientific Publications, Oxford.

Crawford, W. C., Webb, S. C., 2002. Variations in the distribution of magma in the lower crust and at the Moho beneath the East Pacific Rise at 9 degrees-10 degrees N. Earth Planet. Sci. Lett., 203, 117-130.

Detrick, R. S., Buhl, P., Vera, E., Mutter, J., Orcutt, J., Madsen, J., Brocher, T., 1987. Multi-channel seismic imaging of a crustal magma chamber along the East Pacific Rise. Nature, 326, 35-41.

Dodson, M. H., 1986. Closure profiles in cooling systems. Material Sci. Forum, 7, 145-154.

Dohmen, R., Chakraborty, S., 2003. Mechanism and kinetics of element and isotopic exchange mediated by a fluid phase. Am. Mineral., 88, 1251-1270.

Dunn, R. A., Toomey, D. R., Solomon, S. C., 2000. Three-dimensional seismic structure and physical properites of the crust and shallow mantle beneath the East Pacific Rise at 9°30'N. J. Geophys. Res., 105, 23537-23555.

Faak, K., Chakraborty, S., Coogan, L. A., 2013. Mg in plagioclase: Experimental calibration of a new geothermometer and diffusion coefficients. Geochim. Cosmochim. Acta, 123, 195-213.

Faak., K., Coogan, L. A., Chakraborty, S., 2014. A new Mg-in-plagioclase geospeedometer for the determination of cooling rates of mafic rocks. Geochim. Cosmochim. Acta, 140, 691-707.

France, L., Ildefonse, B., Koepke, J., 2009. Interactions between magma and hydrothermal system in Oman ophiolite and in IODP Hole 1256D:

Fossilization of a dynamic melt lens at fast spreading ridges. Geochem. Geophys. Geosys., 10, DOI:10.1029/2009GC002652.

Francheteau, J., Armijo, R., Cheminee, J. L., Hekinian, R., Lonsdale, P., Blum, N., 1990. 1 Ma East Pacific Rise oceanic crust and uppermost mantle exposed by rifting in Hess Deep (equatorial Pacific Ocean). Earth Planet. Sci. Lett., 101, 281-295.

Francheteau, J., Patriat, P., Segoufin, J., Armijo, R., Doucoure, M., Yelleschaouche, A., Zukin, J., Calmant, S., Naar, D. F., Searle, R. C., 1988. Pito and Orongo Fracture-Zones - the Northern and Southern Boundaries of the Easter Microplate (Southeast Pacific). Earth Planet. Sci. Lett., 89, 363-374.

Ghiorso, M. S. and Sack, R. O., 1995. Chemical mass transfer in magmatic processes IV. A revised and internally consistent thermodynamic model for the interpolations of liquid-solid equilibria in magmatic systems at elevated temperatures and pressures. *Contrib. Mineral. Petrol.* **119**, 197-212.

Gillis, K. M., Muehlenbachs, K., Steward, M., Gleeson, T., Karson, J., 2001. Fluid flow patterns in fast spreading East Pacific Rise crust exposed at Hess Deep. J Geophys. Res., 106, 26311-26329.

Gillis, K.M. 1995. Controls on hydrothermal alteration in a section of fast-spreading oceanic crust. Earth Planet. Sci. Lett. 134, 473-489.

Han, S., Carbotte, S. M., Carton, H., Mutter, J. C., Aghaei, O., Nedimovic, M. R., Canales, J. P., 2014. Architecture of on-and off-axis magma bodies at EPR 9°37–40' N and implications for oceanic crustal accretion. Earth Planet. Sci. Lett. 390, 31-44.

Harding, A. J., Orcutt, J. A., Kappus, M. E., Vera, E. E., Mutter, J. C., Buhl, P., Detrick, R. S., Brocher,T. M., 1989. Structure of yound oceanic crust at 13°N on the East Pacific Rise from expanding spread profiles. J. Geophys. Res. 94, 12,163-12,196.

Hasenclever, J., Theissen-Krah, S., Rüpke, L. H., Morgan, J. P., Iyer, K., Petersen, S., Devey, C. W., 2014. Hybrid shallow on-axis and deep off-axis hydrothermal circulation at fast-spreading ridges. Nature, 508, 508-512.

Hekinian, R., Francheteau, J., Armijo, R., Cogne, J. P., Constantin, M., Girardeau, J., Hey, R., Naar, D. F., Searle, R., 1996. Petrology of the Easter microplate region in the South Pacific. J. Volcan. Geotherm. Res., 72, 259-289.

Henstock, T. J., Woods, A. W., White, R. S., 1993. The accretion of oceanic crust by episodic sill intrusion. J. Geophys. R., 98, 4143-4161.

Hey, R. N., Johnson, P. D., Martinez, F., Korenaga, J., Somers, M. L., Huggett, Q. J., Lebas, T. P., Rusby, R. I., Naar, D. F., 1995. Plate boundary reorganization at a large-offset, rapidly propagating rift. Nature, 378, 167-170.

Karson, J. A., Klein, E. M., Hurst, S. D., Lee, C., Rivizzigno, P., Curewitz, D., Morris, A. R., and Hess Deep Science Party, 2002. Structure of uppermost fast-spread oceanic crust exposed at the Hess Deep Rift: Implications for subaxial processes at the East Pacific Rise. Geochem. Geophy.s Geosys., 3, DOI:10.1029/2001GC000155.

Kelemen, P. B., Koga, K., Shimizu, N., 1997. Geochemistry of gabbro sills in the crust-mantle transition zone of the Oman ophiolite: implications for the origin of the oceanic lower crust. Earth Planet. Sci. Lett., 146, 475-488.

Koepke, J., Christie, D. M., Dziony, W., Holtz, F., Lattard, D., Maclennan, J., Park, S., Scheibner, B., Yamasaki, T., Yamazaki, S., 2008. Petrography of the dike-gabbro transition at IODP Site 1256 (equatorial Pacific): The evolution of the granoblastic dikes. Geochem. Geophys. Geosys., 9, DOI:10.1029/2008GC001939.

Korenaga, J., Kelemen, P. B., 1997. Origin of gabbro sills in the Moho transition zone of the Oman ophiolite: Implications for magma transport in the oceanic crust. J.Geophys. Res., 102, 27729-27749.

Lasaga, A. C., 1983. Geospeedometry: an extension of geothermometry, in: Saxena, S. K. (ed), Kinetics and equilibrium in mineral reactions, pp. 82-114, Springer-Verlag, New York.

Lister, C.R.B., 1974. On the penetration of water into hot rock. Geophys. J. R. Astr. Soc., 39: 465-509.

Lonsdale, P., 1988. Structural pattern of the Galapagos microplate and evolution of the Galapagos Triple Junctions. J. Geophys. Res., 93, 13551-13574.

Maclennan, J., Hulme, T., Singh, S. C., 2005. Cooling of the lower oceanic crust. Geology, 33, 357-360.

Mackwell, S. J., Zimmerman, M. E., Kohlstedt, D.L., 1998. High-temperature deformation of dry diabase with application to tectonics on Venus. J. Geophys. Res., 103, 975-984.

Marjanovic, M., Carbotte, S. M., Carton, H., Nedimovic, M. R., Mutter, J. C., Canales, J.P., 2014. A multi-sill magma plumbing system beneath the axis of the East Pacific Rise. Nature Geosciences, 7, 825-829.

Morton, J., Sleep, N.H, 1985. A mid-ocean ridge thermal model: Constraints on the volume of axial hydrothermal heat flux. J. Geophys. Res., 90, 11345-11353.

Onorato P. I. K., Hopper R. W., Yinnon H., Uhlmann D. R., Taylor L. A., Garrison J. R. and Hunter R.H., 1981. Solute partitioning under continuous cooling conditions as a cooling rate indicator. J. Geophys. Res. 86, 9511–9518.

Perk, N.W., Coogan, L. A., Karson, J. A., Klein, E. M., Hanna, H.D., 2007. Primitive cumulates from the upper crust formed at the East Pacific Rise. Contrib. Min. Petrol., 154, 575-590.

Phipps Morgan, J., Chen, Y. J., 1993. The Genesis of oceanic crust - magma injection, hydrothermal cooling, and crustal flow. J. Geophys. Res., 98, 6283-6297.

Quick, J. E., Denlinger, R. P., 1993. Ductile deformation and the origin of layered gabbro in ophiolites. J. Geophys. Res., 98, 14015-14027.

Sano, T., Sakuyama, T., Ingle, S., Rodriguez, S., Yamasaki, T., 2011. Petrological relationships among lavas, dikes, and gabbros from Integrated Ocean Drilling Program Hole 1256D: Insight into the magma plumbing system beneath the East Pacific Rise. Geochem. Geophys. Geosys., 12, DOI:10.1029/2011GC003548.

Turcotte, D. L., Schubert., G., 2002. Geodynamics, second ed. Cambridge University Press. Cambridge.

VanTongeren, J. A., Kelemen, P. B., Hanghoj, K., 2008. Cooling rates in the lower crust of the Oman ophiolite: Ca in olivine, revisited. Earth Planet. Sci. Lett., 267, 69-82.

Van Orman, J. A., Cherniak, D. J., and Kita, N. T., 2014. Magnesium diffusion in plagioclase: Dependence on composition, and implications for thermal resetting of the 26Al–26Mg early solar system chronometer. Earth Plant. Sci. Lett. 385, 79-88.

Von Damm, K. L., 2000. Chemistry of hydrothermal vent fluids from 9° - 10°N, east Pacific Rise: "Time zero", the immediate posteruptive period. J. Geophys. Res. 105, 11203-11222.

Webb, S. P., 2008. Is there a deep hydrothermal circulation at the EPR? Eos Trans. AGU, Fall Meet. Suppl., Abstract B21A-0327.

Wilson, D. S. et al., 2006. Drilling into gabbro in intact ocean crust. Science, 312, 1016-1020.

Table Captions

Table 1. Summary of the cooling rates that were obtained from each Mg-profile in plagioclase from the three sample suites. The sample depth is given in m below the DGB (mbDGB) of the individual sample suite. The given temperature range refers to the *T*-interval over which the diffusion process was modeled (see Section 4.2 and Appendix B for details). *italics* = the observed Mg-profile is very homogeneous, so that only a maximum estimate of the cooling rate can be obtained.

Figure Captions

Fig. 1. Schematic sketch to illustrate how different modes of heat extraction and crystallization in the lower oceanic crust result in different trends for cooling rates as a function of depth. Panel (a) shows a gabbro glacier type model that assumes most of the latent heat to be released in the AML and removed by hydrothermal circulation above this body. To emphasize the potential for heat conduction to be the dominant process of heat removal in the off-axis region in this model the green line in the middle panel shows this scenario. It should be noted that the gabbro glacier crustal accretion model is also permissive of efficient off-axis hydrothermal cooling (e.g. Phipps Morgan and Chen, 1993; Hasenclever et al., 2014). Panel (b) shows a sheeted sill type model that assumes less efficient heat extraction above the AML and more efficient heat extraction by off-axis hydrothermal circulation in the lower crust. The middle panel compares (schematically and not to scale) the expected trends for vertical variation of cooling rate in these hypothetical models with different

efficiencies of hydrothermal cooling at depth. (For interpretation of the references to color in this figure, the reader is referred to the online version of this article.)

Fig. 2. Geographical and structural maps with locations of the three sample sites. (a) Overview of the location of the Hess Deep, the Pito Deep, and IODP drill Site 1256D (red marks). (b) Map of the Galapagos triple junction in the eastern equatorial Pacific Ocean showing major tectonic boundaries and the location of the Hess Deep Rift (red box). (c) Map of the Easter Microplate in the southern Pacific Ocean showing major tectonic boundaries and the location of the Pito Deep (red box). (d and e) Simplified geological map of the Northern wall of the Hess Deep Rift showing the dive tracks with general lithological units and sample locations (based on Gillis et al., 2001). The blue dashed line represents the inferred location of the DGB in this area and the blue shaded area represents a region where only gabbroic rocks were mapped along dive tracks. Contour lines represent depth below sea level given in meters. (f and g) Simplified geological map of the Pito Deep area B showing the dive tracks with general lithological units and sample location (based on Perk et al., 2007). Base maps in (a)-(c) were created with GeoMapApp. (For interpretation of the references to color in this figure, the reader is referred to the online version of this article.)

Fig. 3. Examples of the different Mg-profile shapes observed in plagioclase in samples from different depth below the DGB (in meters, gray numbers besides the boxes) from Hess Deep (left column) and Pito Deep (right column). Open circles show the Mg-concentrations that were measured along full profiles in plagioclase. Solid pink lines show the modeled diffusion profile that matches best with the measured profile. The inset in each box shows the X_{An}-content that was measured

along the same transect as the Mg-profile. (For interpretation of the references to color in this figure, the reader is referred to the online version of this article.)

Fig 4. Diagram to show the obtained cooling rates (plotted as log d*T*/*dt*) versus the sample depth below the DGB. Arrows indicate that only maximum cooling rates could be obtained, because the measured Mg-profiles were homogeneous (see text for discussion). Light pink symbols show data from sample 022005-1052 that is regarded as an outlier (see text for discussion). For comparison, cooling rates obtained from the *Ca-in-olivine geospeedometer* (Coogan et al., 2007) are shown for the depth range, where data from that study is available. (For interpretation of the references to color in this figure, the reader is referred to the online version of this article.)

Fig. 5. Comparison of the cooling rates obtained from diffusion modeling of Mg in plagioclase in the natural samples with different thermal models. M = cooling rates from Maclennan et al. (2005) obtained from a thermal model with a thermal diffusivity of 8 x 10^{-7} m^2s^{-1} and various amounts of hydrothermal cooling off-axis (50-71 kWm^{-1}; only their model 4 has no hydrothermal cooling off-axis). D = cooling rates calculated from the isotherms separation of Dunn et al. (2000) for a cooling interval of 1000-600°C. H = cooling rates calculated from the isotherm separation of Hasenclever et al. (2014) for a cooling interval of 1000-600°C. T&S = simple conductive half-space model based on Eq. 4.124 in Turcotte and Schubert (2002) with a thermal diffusivity of 1 x $10^{-6}m^2s^{-1}$. The top of the lower crust (i.e. the dike/gabbro boundary) is held at a constant temperature of 400°C, i.e. the temperature in the dikes is assumed to be 400°C (based on temperature estimates for hydrothermal fluids (e.g. Von Damm, 2000) and from petrology of alteration of dikes (e.g. Gillis, 1995) in the

area). The initial temperature of the entire crust and upper mantle is assumed to be 1300°C. Cooling rates are extracted for the *T*-interval of 900-600°C and 700-600°C. Tini layered = conductive cooling model with a layered initial temperature distribution. The temperature at the top (= seafloor and lava) is held constant at 4°C. The initial temperature profile is set based on the expected profile at the edge of the AML as follows: layer 1 (dikes): 1 km thick, 400°C; layer 2 (gabbros): 4 km thick, 1250°C; layer 3 (upper mantle): 15 km thick, 1300°C. Conductive cooling was modeled from these initial and boundary conditions and cooling rates were extracted at around 900°C for all depth and around the average obtained rim closure temperature (Tc_{rim}) for each sample depth of the Hess Deep (HD) and Pito Deep (PD) sample suite. Note that the difference between the conductive model 4 from Maclennan et al., 2005, and the other conductive models results from the fact that their model 4 is a 2D model that additionally considers horizontal heat transport, and latent heat of crystallization. (For interpretation of the references to color in this figure, the reader is referred to the online version of this article.)

Fig. 6. Diagram to illustrate a bounding constraint on the thermal structure in the lower crust in the off-axis region. For each sample depth, the average cooling rate obtained from the *Mg-in-plagioclase geospeedometer* was used to determine the time needed to cool from (Tc_{rim} + 100°C) to Tc_{rim}. The distance the crust would move in this time was calculated assuming a half spreading rate of 65 mmy^{-1} to yield the horizontal separation of two isotherms that are 100°C apart. In order to locate the limiting distance from the ridge at which these temperatures may be attained, cooling above (Tc_{rim} + 100°C) was assumed to be instantaneous (i.e. (Tc_{rim} + 100)°C is assumed to be attained at zero time at the ridge axis itself at the respective depths).

Thus, these values provide a minimum constraint on the time needed for the crust to cool down to Tc_{rim} at a given depth, and the distance from the ridge where this may be attained for the known spreading velocity. The bold green and blue lines represent the minimum time (and equivalently, distance) required to cool down to 750°C, 700°C and 650°C respectively, at depths where information on cooling rates around each of these temperatures has been frozen in the plagioclase record. An alternate, less extreme case is where cooling occurs linearly from the solidus temperature of ~1200°C to Tc_{rim}. Tc_{rim} at any given depth is attained much later (at a greater distance from the ridge) in this case and tips of horizontal arrows drawn at each depth mark these points. Thus, for any conceivable cooling history, the inferred temperature at a given depth has to lie within the gray region to be consistent with the thermal history recorded in the plagioclase crystals. For comparison, the position of the 1000-400°C isotherms from Hasenclever et al. (2014) (marked "H") for the depth interval corresponding to our study are shown. (For interpretation of the references to color in this figure, the reader is referred to the online version of this article.)

Fig B1. Illustration of the effect of the choice of modeling scenario on the obtained cooling rate. The diagrams show synthetic Mg-concentration profiles for three different plagioclase crystals (P1 = weekly curved Mg-profile; P2 = homogeneous Mg-profile at 0.4 wt% MgO and P3 = homogeneous Mg-profile at 0.2 wt% MgO). For simplicity, all plagioclase crystals are assumed to have homogeneous X_{An} = 0.6 and to be in contact with Cpx with 14 wt% MgO. The silica activity of the system is assumed to be constraint by the assemblage Ol+Opx. The pink bold lines show best fit profiles for modeling scenario (A), i.e., Tc_{rim} can be obtained using Eq. (4) from Faak et al. (2014) with the Mg-concentration at the rim of the plagioclase. The light pink bold lines show best fit profiles for modeling scenario (B), i.e., modeling is continued to 600°C, but at temperature T_{closed} ($Tc_{rim} > T_{closed} > 600°\mathrm{C}$), the system was modeled with closed boundaries (see text for discussion). (For interpretation of the references to color in this figure, the reader is referred to the online version of this article.)

Highlights

- We use diffusion modeling of Mg in plagioclase to determine cooling rates
- Cooling rates were obtained from natural samples of the lower oceanic crust
- Obtained cooling rates significantly decrease with increasing sample depth
- Our data is best explained by conductive thermal models
- Our data is inconsistent with substantial cooling by off-axis hydrothermal circulation

Figure 1

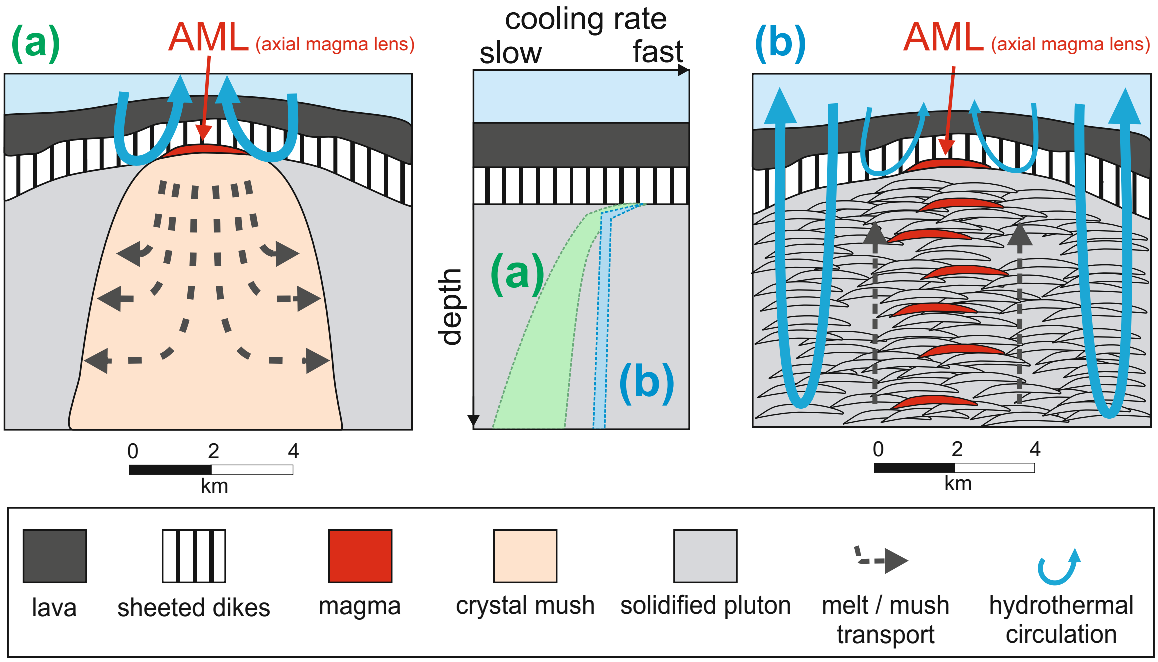
(a)
AML (axial magma lens)
0 2 4
km
cooling rate
slow
fast
depth
(a)
(b)
(b)
AML (axial magma lens)
0 2 4
km
lava
sheeted dikes
magma
crystal mush
solidified pluton
melt / mush transport
hydrothermal circulation

Figure 2

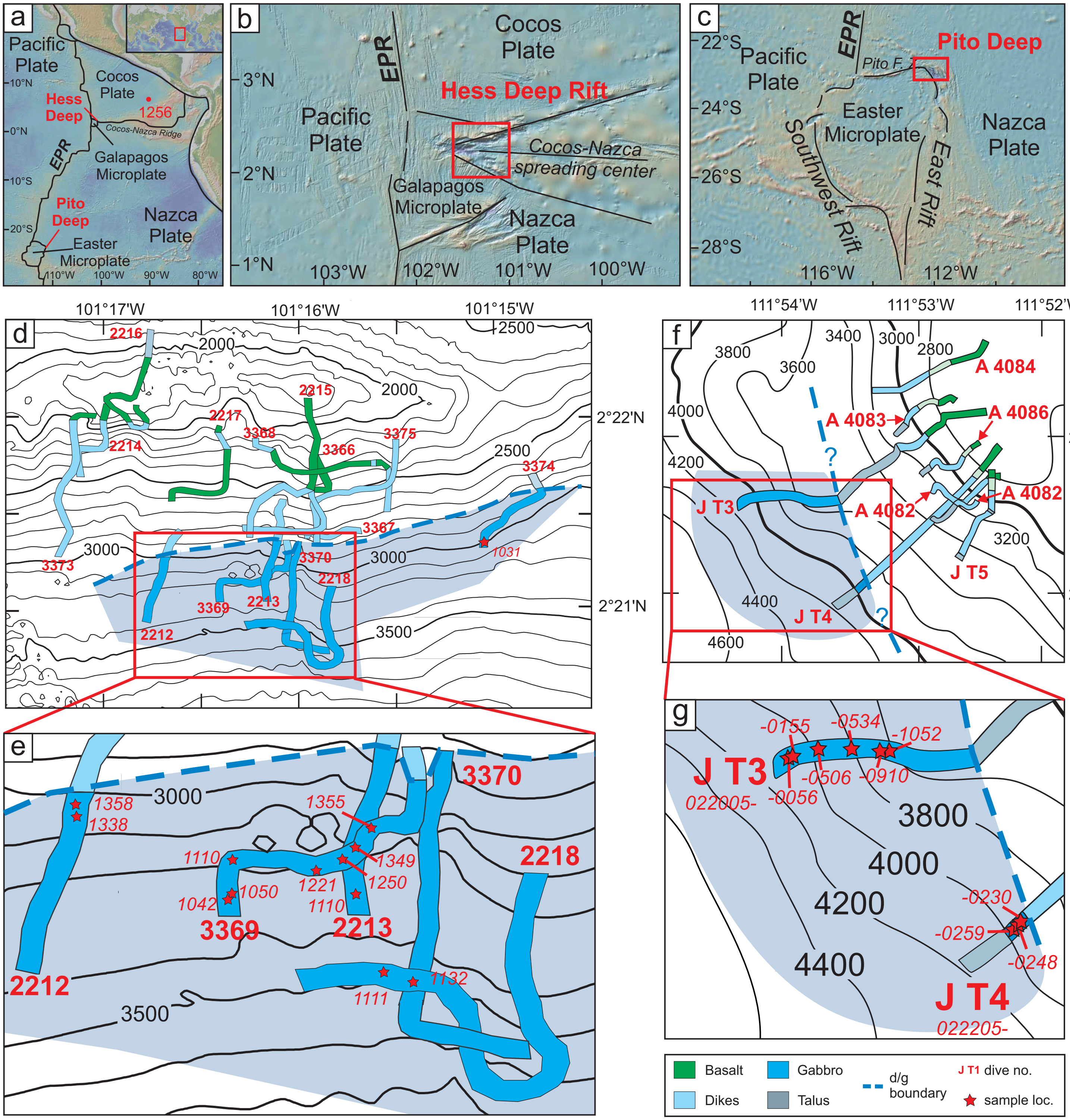
a
Pacific Plate
Cocos Plate
Hess Deep
1256
Cocos-Nazca Ridge
EPR
Galapagos Microplate
Pito Deep
Nazca Plate
Easter Microplate
10°N
0°N
10°S
20°S
110°W
100°W
90°W
80°W
b
Cocos Plate
EPR
Hess Deep Rift
Pacific Plate
Cocos-Nazca spreading center
Galapagos Microplate
Nazca Plate
3°N
2°N
1°N
103°W
102°W
101°W
100°W
c
Pacific Plate
EPR
Pito F.
Pito Deep
Easter Microplate
Nazca Plate
Southwest Rift
East Rift
22°S
24°S
26°S
28°S
116°W
112°W
d
101°17'W
101°16'W
101°15'W
2°22'N
2°21'N
2000
2500
3000
3500
2216
2215
2217
3368
3375
2214
3366
3374
3367
3373
3370
2218
1031
3369
2213
2212
e
3000
3500
3370
2218
3369
2213
2212
1358
1338
1355
1349
1250
1110
1221
1110
1050
1042
1132
1111
f
111°54'W
111°53'W
111°52'W
22°58'S
22°59'S
3800
3600
3400
3000
2800
4000
4200
4400
4600
3200
A 4084
A 4083
A 4086
A 4082
A 4082
J T3
J T4
J T5
?
?
g
-0155
-0534
-1052
-0506
-0910
-0056
J T3
022005-
3800
4000
4200
4400
-0230
-0259
-0248
J T4
022205-
🟩 Basalt
🟦 Gabbro
d/g boundary
J T1 dive no.
Dikes
Talus
★ sample loc.

Figure 3

Click here to download Figure: Fig3_Profiles.eps

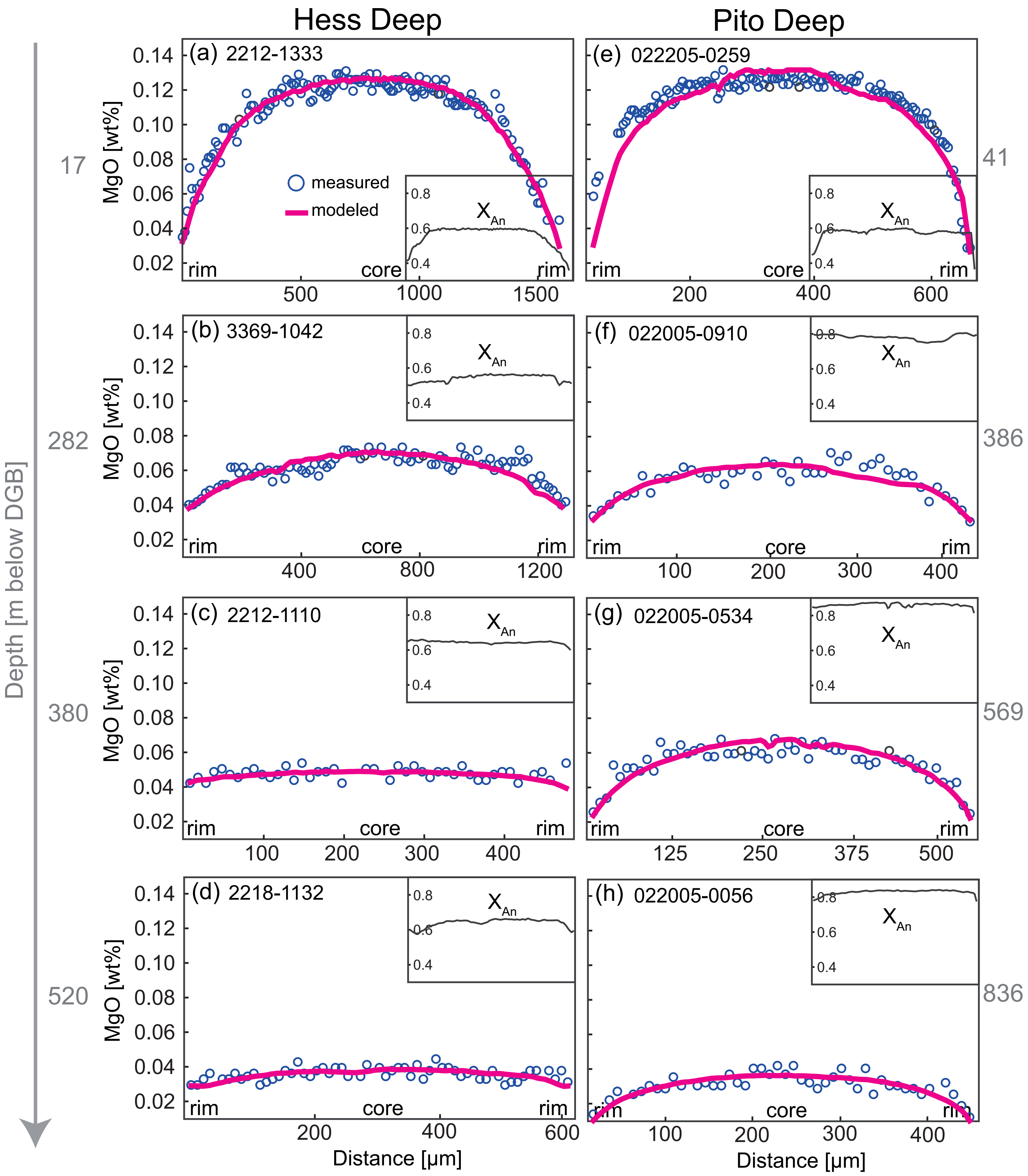

Figure 4

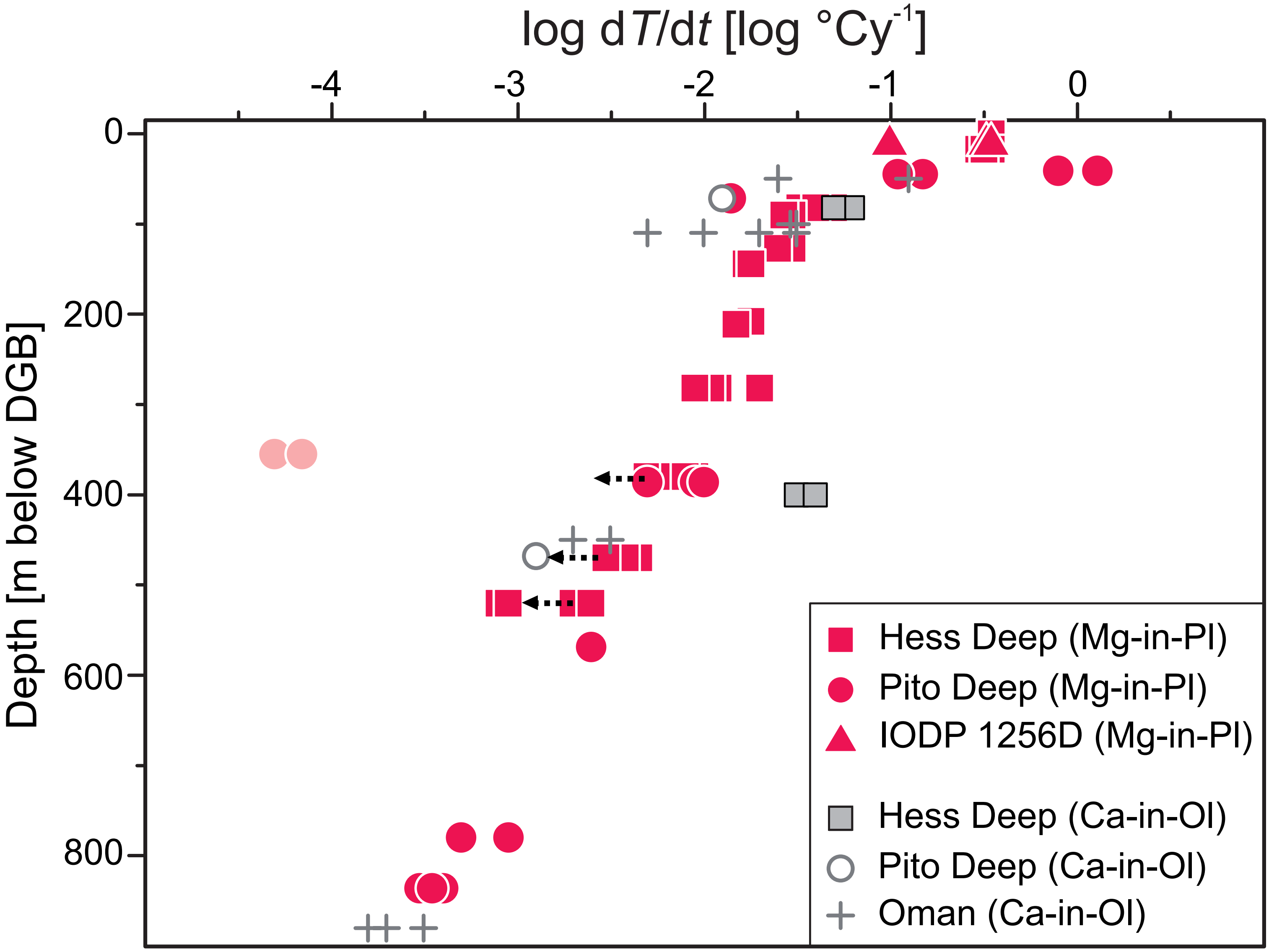
log dT/dt [log °Cy^{-1}]
-4
-3
-2
-1
0
Depth [m below DGB]
0
200
400
600
800
■ Hess Deep (Mg-in-Pl)
● Pito Deep (Mg-in-Pl)
▲ IODP 1256D (Mg-in-Pl)
■ Hess Deep (Ca-in-Ol)
○ Pito Deep (Ca-in-Ol)
+ Oman (Ca-in-Ol)

Figure 5

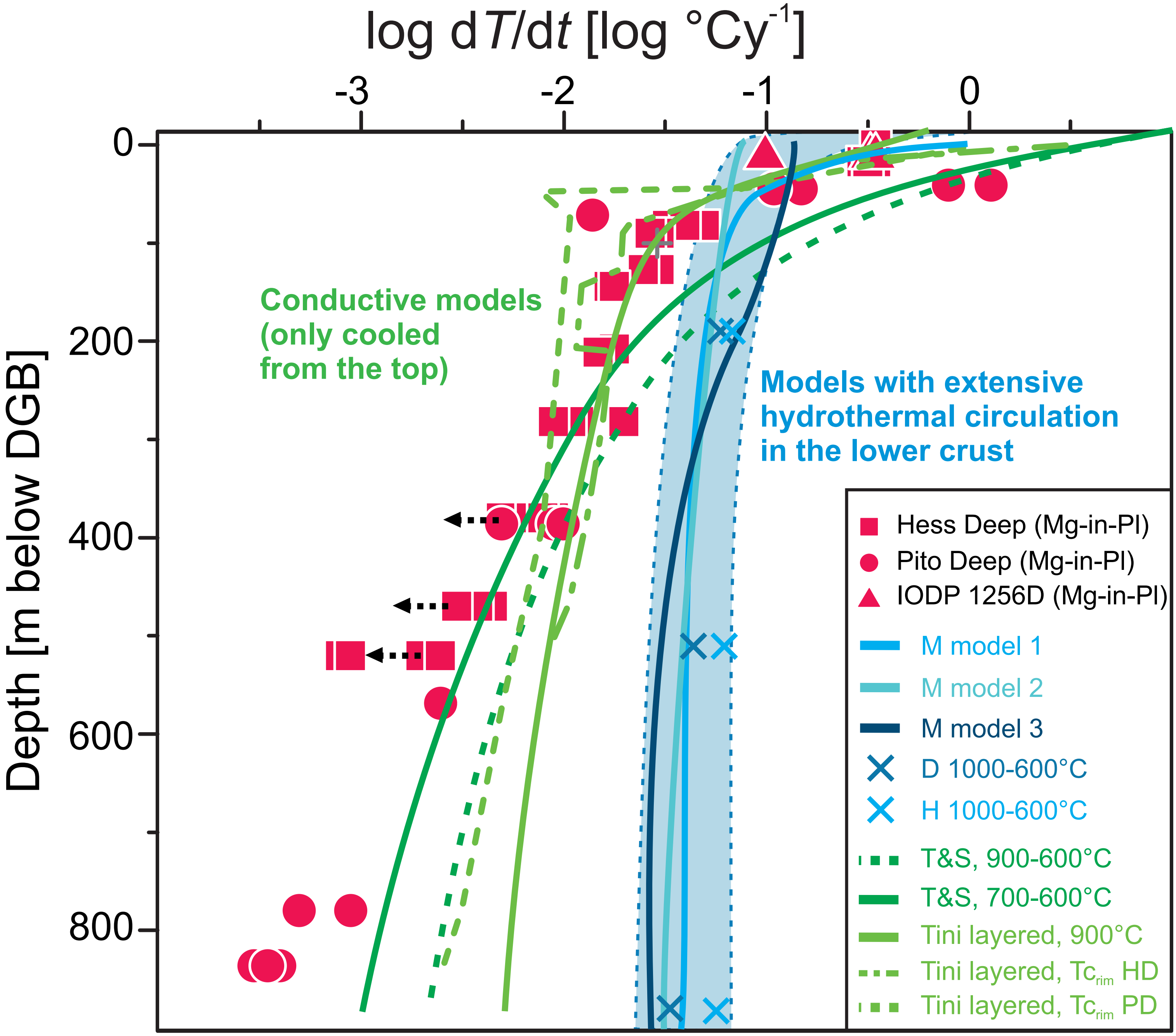
log d*T*/dt [log °Cy^{-1}]
-3
-2
-1
0
Depth [m below DGB]
0
200
400
600
800
Conductive models (only cooled from the top)
Models with extensive hydrothermal circulation in the lower crust
Hess Deep (Mg-in-Pl)
Pito Deep (Mg-in-Pl)
IODP 1256D (Mg-in-Pl)
M model 1
M model 2
M model 3
D 1000-600°C
H 1000-600°C
T&S, 900-600°C
T&S, 700-600°C
Tini layered, 900°C
Tini layered, Tc$_{rim}$ HD
Tini layered, Tc$_{rim}$ PD

Figure 6

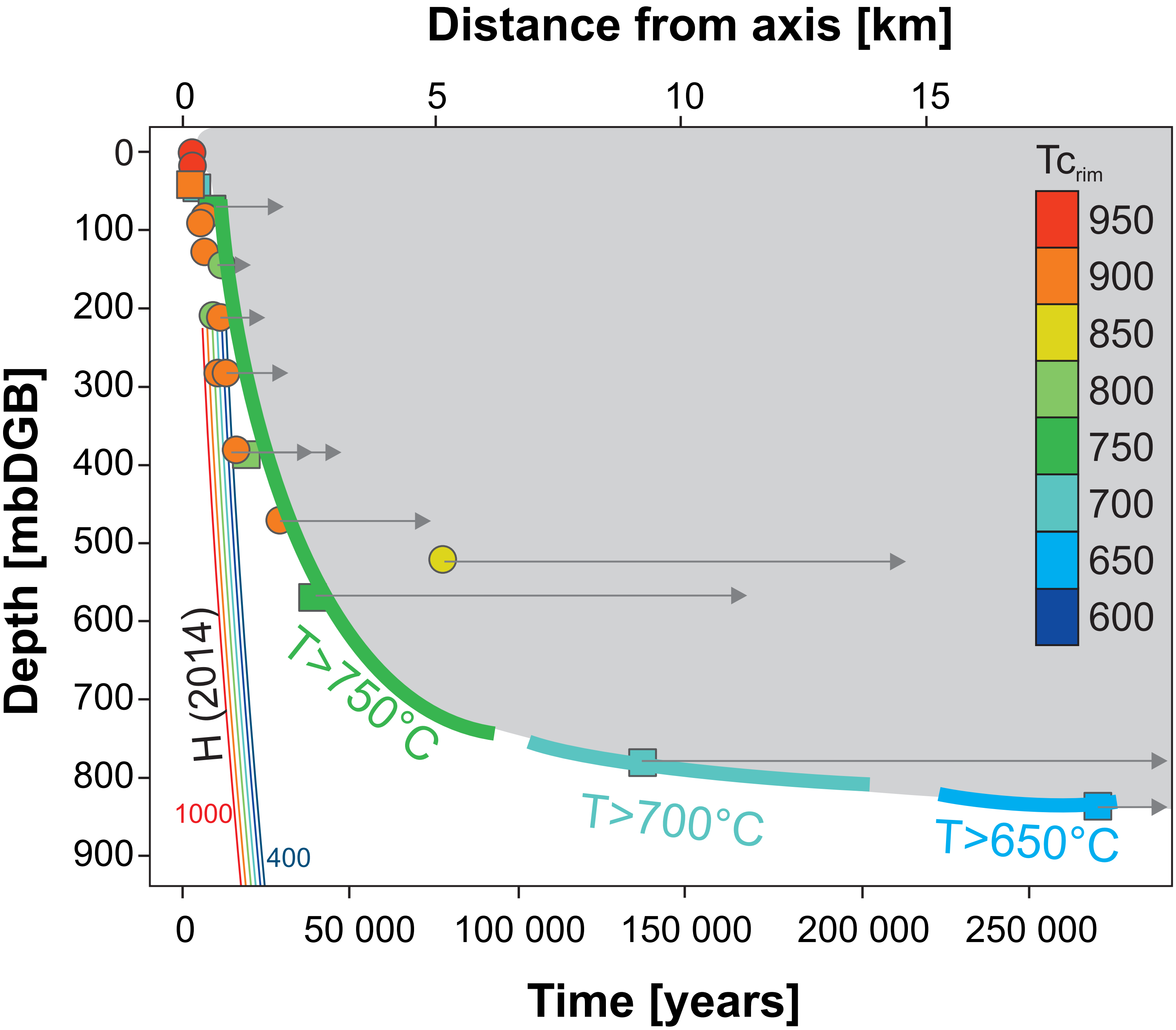
Distance from axis [km]
0
5
10
15
Depth [mbDGB]
0
100
200
300
400
500
600
700
800
900
Time [years]
0
50 000
100 000
150 000
200 000
250 000
Tc$_{rim}$
950
900
850
800
750
700
650
600
H (2014)
1000
400
T>750°C
T>700°C
T>650°C

Figure A1

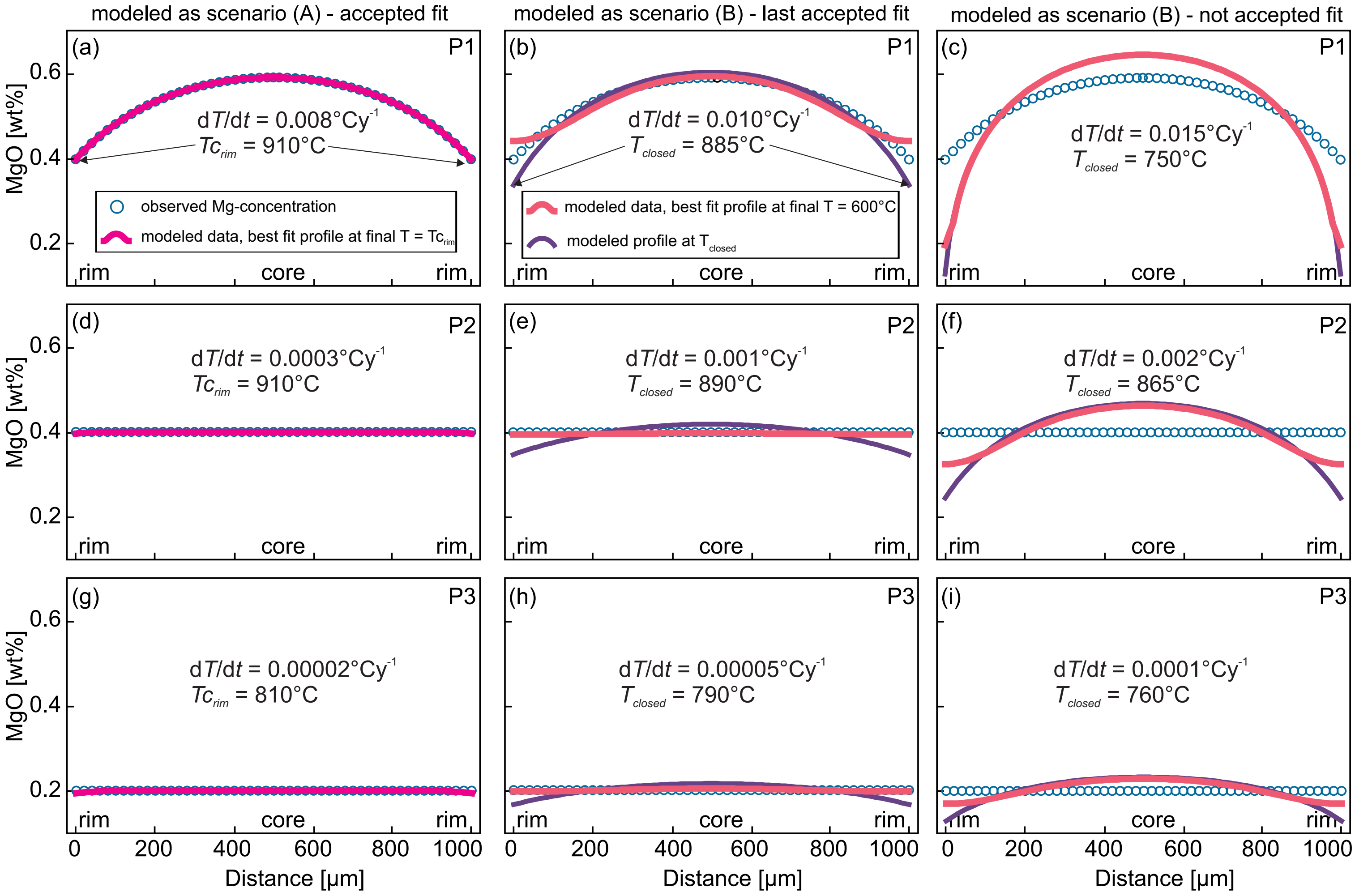
modeled as scenario (A) - accepted fit
modeled as scenario (B) - last accepted fit
modeled as scenario (B) - not accepted fit
(a)
P1
dT/dt = 0.008°Cy-1
Tc_rim = 910°C
observed Mg-concentration
modeled data, best fit profile at final T = Tc_rim
(b)
P1
dT/dt = 0.010°Cy-1
T_closed = 885°C
modeled data, best fit profile at final T = 600°C
modeled profile at T_closed
(c)
P1
dT/dt = 0.015°Cy-1
T_closed = 750°C
(d)
P2
dT/dt = 0.0003°Cy-1
Tc_rim = 910°C
(e)
P2
dT/dt = 0.001°Cy-1
T_closed = 890°C
(f)
P2
dT/dt = 0.002°Cy-1
T_closed = 865°C
(g)
P3
dT/dt = 0.00002°Cy-1
Tc_rim = 810°C
(h)
P3
dT/dt = 0.00005°Cy-1
T_closed = 790°C
(i)
P3
dT/dt = 0.0001°Cy-1
T_closed = 760°C
MgO [wt%]
0.6
0.4
0.2
rim
core
rim
0
200
400
600
800
1000
Distance [μm]

Table 1

Table 1. Summary of the cooling rates that were obtained from each used Mg-profile in the individual plagioclase crystals from the three sample suites. The sample depth is given in m below the DGB of the individual sample suite (mbDGB). The given temperature range refers to the *T*-interval over which the diffusion process was modeled (see Section 4.2 and Appendix I for details). *italics* = the observed Mg-profile is very homogeneous, so that only a maximum estimate of the cooling rate can be obtained.

Sample	Depth [mbDGB]	Plag	Profile	Length [µm]	dT/dt [°C/y]	log dT/dt	T-interval [°C]
				Hess Deep			
2212-1358	0	Pl4	2	610	0.35	-0.46	1155-960
2212-1338	17	Pl1	1	500	0.35	-0.46	1133-940
2212-1338	17	Pl3	1	1590	0.3	-0.52	1223-950
2212-1338	17	Pl3	2	1550	0.32	-0.49	1221-800
3369-1355	82	Pl1	2	860	0.05	-1.30	1179-980
3369-1355	82	Pl3	1	530	0.033	-1.48	1145-870
3369-1355	82	Pl3	2	380	0.04	-1.40	1121-900
3369-1349	90	Pl1	1	590	0.03	-1.52	1152-900
3369-1349	90	Pl3	2	350	0.027	-1.57	1115-890
3374-1031	127	Pl1	1	590	0.028	-1.55	1152-920
3374-1031	127	Pl1	2	260	0.03	-1.52	1094-910
3374-1031	127	Pl2	2	250	0.025	-1.60	1092-920
3369-1250	144	Pl1	1	265	0.017	-1.77	1096-840
3369-1250	144	Pl2	1	190	0.018	-1.74	1072-820
3369-1221	208	Pl1	1	207	0.018	-1.74	1078-830
3369-1110	211	Pl1	1	460	0.015	-1.82	1135-920
3369-1050	282	Pl2	2	660	0.02	-1.70	1160-900
3369-1050	282	Pl3	1	960	0.01	-2.00	1187-950
3369-1050	282	Pl3	2	450	0.012	-1.92	1133-930
3369-1042	282	Pl1	1	1410	0.011	-1.96	1211-920
3369-1042	282	Pl1	2	1590	0.009	-2.05	1223-890
2213-1110	380	Pl2	1	640	0.005	-2.30	1158-940
2213-1110	*380*	*Pl3*	*1*	*470*	*0.007*	*-2.15*	*1136-915*
2213-1110	380	Pl4	2	510	0.009	-2.05	1142-920
2213-1110	380	Pl6	2	560	0.008	-2.10	1149-920
2218-1111	*470*	*Pl1*	*1*	*350*	*0.0045*	*-2.35*	*1115-910*
2218-1111	*470*	*Pl1*	*2*	*690*	*0.0038*	*-2.42*	*1164-910*
2218-1111	*470*	*Pl2*	*2*	*510*	*0.003*	*-2.52*	*1142-900*
2218-1132	*520*	*Pl2*	*2*	*105*	*0.002*	*-2.70*	*1030-850*
2218-1132	520	Pl3	1	600	0.0008	-3.10	1154-865
2218-1132	*520*	*Pl3*	*2*	*300*	*0.0009*	*-3.05*	*1104-870*
2218-1132	*520*	*Pl5*	*1*	*170*	*0.0025*	*-2.60*	*1064-840*
				Pito Deep			
022205-0259	41	Pl2	1	480	1.3	0.11	1188-930
022205-0259	41	Pl2	2	702	0.8	-0.10	1215-900
022205-0248	45	Pl2	2	888	0.15	-0.82	1182-640
022205-0248	45	Pl4	1	200	0.11	-0.96	1076-720
022205-0230	72	Pl1	1	370	0.014	-1.85	1119-780

022005-1052	355	Pl2	2	420	0.00005	-4.30	1128-730
022005-1052	355	Pl3	2	500	0.00007	-4.15	1141-720
022005-0910	386	Pl1	2	240	0.009	-2.05	1089-835
022005-0910	386	Pl2	2	180	0.01	-2.00	1068-810
022005-0910	386	Pl4	2	460	0.005	-2.30	1135-800
022005-0534	569	Pl2	1	560	0.0025	-2.60	1149-760
022005-0155	780	Pl1	2	830	0.0009	-3.05	1177-710
022005-0155	780	Pl2	1	850	0.0005	-3.30	1178-720
022005-0056	836	Pl2	2	830	0.0004	-3.40	1177-680
022005-0056	836	Pl3	1	470	0.0003	-3.52	1136-690
022005-0056	836	Pl5	1	840	0.00035	-3.46	1178-670
IODP Site 1256D							
216R1 15-20	12.1	Pl3	1	460	0.1	-1.00	1135-860
216R1 49-57	12.4	Pl1	1a	313	0.33	-0.48	1107-810
216R1 49-57	12.4	Pl1	1b	313	0.35	-0.46	1122-820